Multi-laser powder bed fusion of Ti6Al4V: Diode area melting utilizing low-power 450 nm diode lasers

Halil Caglar [*,1], Anqi Liang, Kristian Groom, Kamran Mumtaz

Department of Mechanical Engineering, The University of Sheffield, Sheffield S1 4BJ, United Kingdom

ABSTRACT

Diode Area Melting (DAM) is an innovative approach to laser powder bed fusion. This research for the first time utilized multiple low wavelength (450 nm) and low power lasers (4 W each) to simultaneously process Ti6Al4V from a powder bed, resulting in high density samples (> 99%). The use of nine lasers perpendicular to the scanning direction allowed for the creation of melt pools with widths larger than 1000 μm, reducing the number of passes within a layer compared to traditional single laser LPBF systems. However, the increase in melt pool width creates challenges related to maintaining uniform melt pool penetration depths, this intern creates issues achieving high density in multi-layer parts. A parameter map based on normalized energy density was created. The research also investigated the effect of variable process conditions (scanning speed, hatch distance, and layer height), normalized energy density on densification, microstructure, and hardness. Implementing a rescanning strategy on each layer reduced average surface roughness and increased density while reducing hardness by approximately 40%. X-ray Diffraction analyses showed that the β phase occurred with increased energy density in as-built samples. Coarser lamellar structures were observed in the lower sections due to slower cooling rates, while finer, more martensite structures were observed towards the top, resulting in a basket-weave type microstructure throughout the sample. Furthermore, the lamellar sub-grains were visible without etching. This innovative technology shows that an array of low-power lasers can melt and fuse Ti6Al4V powder to create dense samples.

1. Background

Laser Powder Bed Fusion (LPBF) technology is a method of metal additive manufacturing used to create three-dimensional components by selectively melting deposited powder feedstock. This process produces high-density components with refined microstructures from various engineering alloys such as Ti6Al4V (Ti64). LPBF-produced Ti64 parts are widely used in the aerospace, energy, and medical sectors due to its ability to create fully dense geometrically intricate component with minimal material waste (Shipley et al., 2018). However, LPBF systems face limitations related to scalability, often requiring high laser powers (Zavala-Arredondo et al., 2017). High-intensity, rapidly moving lasers can create significant thermal gradients that may cause major defects in the component (Liu et al., 2016).

An alternative approach to traditional LPBF has been pioneered at The University of Sheffield, involving the use of multiple short-wavelength diode lasers, each operating at 3–5 W of power. This

innovative technology, known as Diode Area Melting (DAM), allows for the complete melting of metal powder feedstock while maintaining enhanced thermal control during the processing (Zavala-Arredondo et al., 2017). In DAM, multiple adjacent diode lasers (with or without arrays) are integrated into a multi-laser head, which then traverses the powder bed in a scanning manner. (as shown in Fig. 1 (derived from (Alsaddah et al., 2021)).

Matthews et al. (2017) explained when absorptivity is low, the metal powder tends to exhibit high reflectivity, which can lead to incomplete melting if the laser power is insufficient. Conversely, high absorptivity facilitates efficient absorption of laser energy, resulting in improved fusion (Alsaddah et al., 2021). indicated that the use of high-power diode lasers with shorter wavelengths can significantly enhance the absorptivity of metal powders. Specifically, when employing an 808 nm diode laser on Ti64, absorptivity can be increased by approximately 13% compared to utilizing a 1064 nm laser. Furthermore, employing 450 nm lasers when processing the titanium alloy Ti64 has demonstrated an
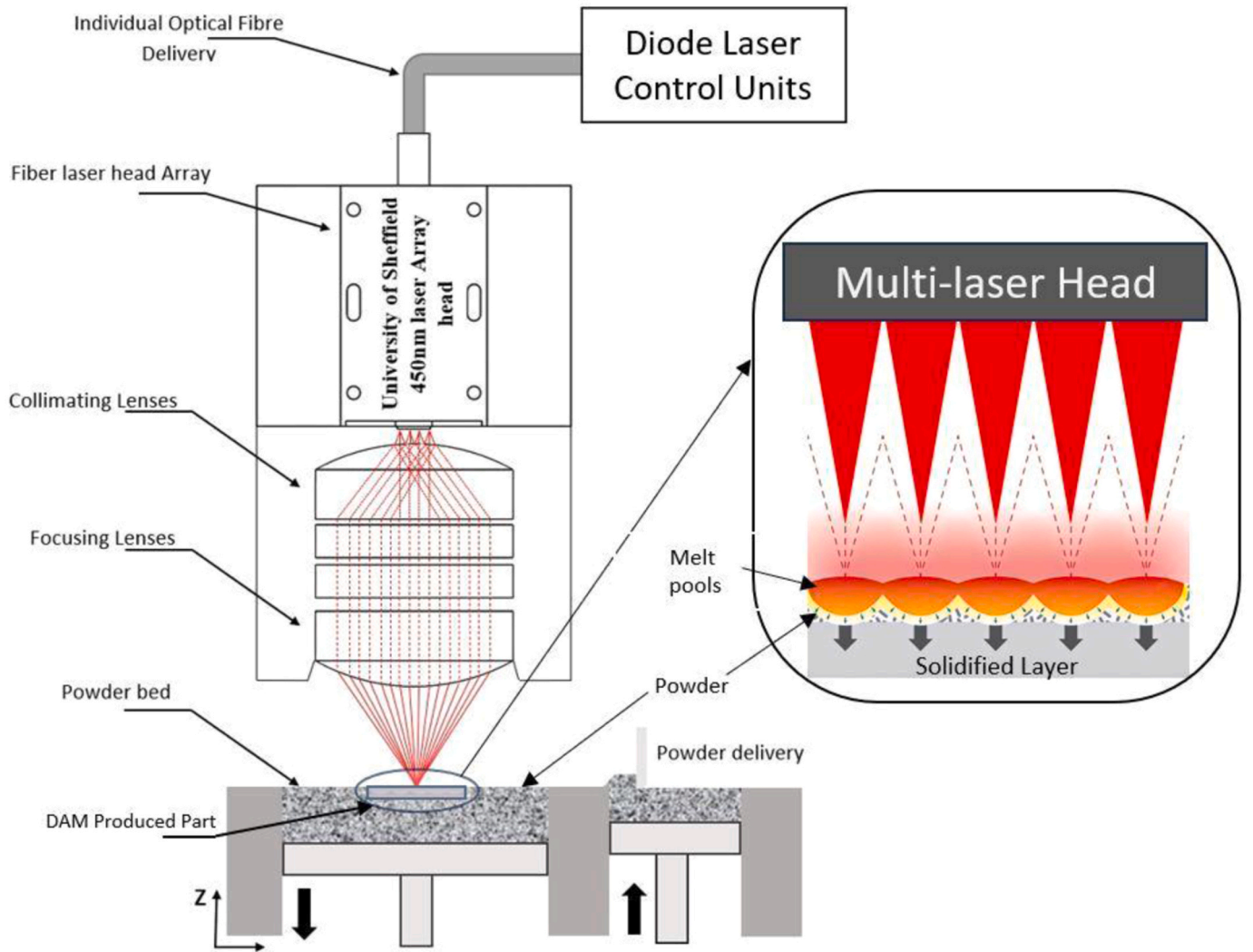
Fig. 1. Blueprints and Visual Depiction of DAM System Elements [4], Including Detailed Representation of Melt Pool and Neighboring Laser Spot Arrangements.

11% increase in absorption compared to 808 nm diode lasers, highlighting the potential of shorter wavelengths in enhancing energy absorption during laser processing tests.

In literature mainly four essential parameters were used to classify energy distribution in the processed area in LPBF, known as volumetric energy density (VED), where laser power, scanning speed, hatch distance (laser overlap), and layer height (Singla et al., 2021). However, a study by (Thomas et al., 2016) conducted an extensive investigation into the factors impacting the microstructure of parts produced through LPBF and created a normalized energy density (NED-E_0^*) equation. Beam quality, focusing, wavelength (therefore, surface absorptivity (coupling coefficient) (A)), particle size distribution (PSD) (the authors assumed PSD of 0.67 and provided an explanation), scanning strategy, oxygen levels within the chamber, the specific heat capacity of the powder (C_p), single laser beam radius (r_b), thermal conductivity, diffusivity, material density, and its melting temperature (T_M), powder bed temperature (T_0), layer height (l) and its normalized version (l^*), hatch distance (h) and its normalized version (h^*), laser power (q) and its normalized version (q^*), and scanning speed (v) and its normalized version (v^*) were among the parameters under consideration. This research showed that parameter dimensionless groups provide a broader explanation than VED. The E^* equation represents the amount of energy needed to raise the local temperature of the powder bed to the melting temperature of the metal during one scan. Eq. (1) shows the final version after iterations with the influenced parameters of the E^* equation, including all other parameter
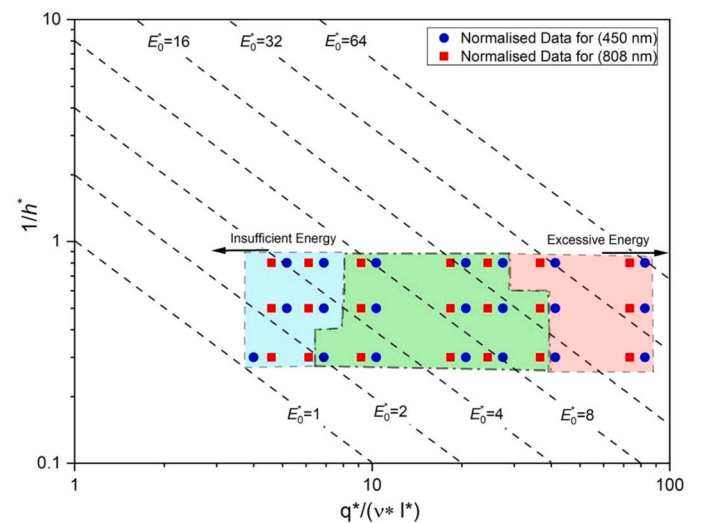

Fig. 2. Analysis of E_0^* Distribution in 450 nm and 808 nm Single Diode Lasers from [4]. The x-axis represents E*, and the y-axis represents, 1/h*, the hatch spacing relative to the diameter of the laser beam, according to [7].
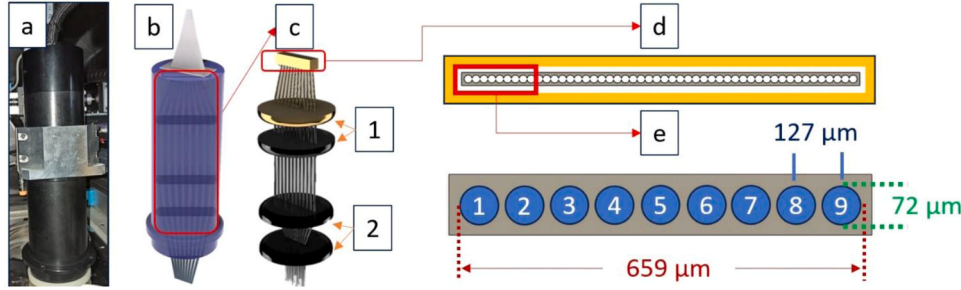
Fig. 3. 450 nm Multi-Laser System Schematics from the Study: (a) Actual Image, (b) 3D Transparent Representation, (c) Inside View with (1) Collimating and (2) Focusing Lenses, (d) 50-Unit Multi-Laser Fiber Connection Slots, (e) Configuration of 9 Installed Lasers with a 127 μm Separation Distance, and Measured Focused Laser Irradiated Area of 659 μm Length and 72 μm Width.

integrations, as explained by (Thomas et al., 2016).

$$E^* = \frac{q^*}{(\nu^* l^*)} = \left[\frac{Aq}{(2\nu l r_b)} \right] \left[\frac{1}{0.67 C_p (T_m - T_0)} \right] \quad (1)$$

In Fig. 2, (Alsaddah et al., 2022) showed the normalized energy density regions in which Ti64 can be processed by using multiple 808 nm 4 W lasers in arrays (E_0^* represents the constant normalized energy density values to raise the melt pool temperature beyond melting temperature with multiple scans (therefore, E_0^* was calculated with the multiplication of E^* and $1/h^*$)). That investigation found that $E_0^* < 4.5$ produced insufficient energy input, creating a lack of fusion between layers, $E_0^* > 14.8$ was generating keyholes due to excessive energy input, and $4.5 < E_0^* < 14.5$ created high-density parts (>95%). However, a modification was made to the beam radius due to the elliptical shaping of the spot by activating multiple beams (the modified beam length along the scanning direction is indicated as $2r_m$). Therefore, they developed Eq. (2) for Eq. (1) to replace r_b in Eq. (1). Furthermore, they changed h^* accordingly (Eq. (3)).

$$2r_m = (n * 2r_b) + ((n - 1) * d_g) \quad (2)$$

$$h^* = h/r_m \quad (3)$$

Where n corresponds to the number of active adjacent lasers and d_g is the space between neighboring lasers (Alsaddah et al., 2022).

Microstructural control, mechanical performance optimization, and residual stress management of manufactured components mainly depend on the resultant cooling rate (Shipley et al., 2018). The cooling rate during SLM can be up to 10^7 °C/s, whilst DAM can generate cooling rates as low as 600 °C/s (Alsaddah et al., 2021) (Alsaddah et al., 2022). explained that during the DAM process of the Ti64, the presence of a higher cooling rate leads to the formation of smaller grain sizes. Specifically, this results in the formation of martensite α' when the high-temperature solidified material crosses the threshold of the martensite start temperature line within a specific time during solidification (Ahmed and Rack, 1998). The martensite phase increases the strength and hardness of the Ti64 but can also increase residual stress, potentially creating cracks and geometric distortion because of the high cooling rate (Song et al., 2012). Alternatively, a slower cooling rate allows for larger grain structures (α, β, $\alpha + \beta$, and Widmanstätten α) and assists in the reduction of residual stress (Ahmed and Rack, 1998). For example, Widmanstätten α generally occurs when the $\alpha + \beta$ alloys are cooled from the parental β section after post-processing (Simonelli et al., 2014). For comparison, the forged Ti64 microstructure is generally in bimodal orientation (Lütjering, 1998). A formation of a microstructure study with LPBF shows that fully lamellar structures occur from the bottom section of the sample to the top (transforming from fully equiaxed, bimodal, lamellar $\alpha + \beta$ to fully martensite α' towards the top layer from a build direction perspective (Simonelli et al., 2014). It shows that the bottom layers were transformed to the $\alpha + \beta$ morphologies due to partial annealing because of the heat cycles and decreased cooling

rate when the number of layers increased (Singla et al., 2021). On the other hand, studies employing rescanning strategies indicate that it can cause the microstructure to become coarser (Liang et al., 2022), creating a decrease in hardness (Xiao et al., 2020), a decrease in overall surface roughness (R_a) (Liang et al., 2022), an increase in density (Liang et al., 2022) and a decrease in residual stress (Ali et al., 2018).

This study aims to analyze the use of a 450 nm laser for processing Ti64 using DAM. A parameter map with normalized energy density will be developed as part of the investigation to establish a standardized framework for cross-system comparison (e.g., LPBF). A focused characterization will be conducted to assess how layer height influences component density and evaluate the influence of rescanning on component density. An exploration into the significance of cooling rate and microstructure will be scrutinized.

2. Methodology

2.1. System development

2.1.1. Multi-laser head and laser beam characteristics

The bespoke DAM process uses collimating and focusing lenses (Figs. 3-c1-c2) within a multi-laser head assembly to achieve localized melting. To ensure compatibility with 450 nm investigations, a newly integrated multi-laser head was employed for this experiment. This advanced system has the capacity to accommodate up to 50 laser fibers in a laser light-tight shell, as illustrated in Fig. 3-a-b-c-d. These laser fibers are strategically spaced at intervals of 127 μm (Fig. 3-e) at a fixed focal length of 60 mm ± 3 mm.

For the purposes of this study, a configuration employing only nine lasers from the Beijing Reful Co. RH450–45-105-FC/PC with a maximum of 36 W in total (Fig. 3-d-e). The size and configuration of the lasers were measured using the NanoScan2sPryo/9/5 profilometer. Throughout the data-collecting process, the laser power was consistently set to 0.7 A, yielding an approximate power output of 1 W per laser, with a minimal deviation of ± 0.1 W. Each specific laser was shown as a single spot with a size of $72 \times 72 \pm 1$ μm and the beam size of an array of nine adjacent lasers was 659 μm in length and 72 μm width at the Full Width at Half Maximum (FWHM) (Fig. 3-e). It's important to acknowledge that the laser-irradiated area of the nine-laser setup seemed non-uniform and elliptical. A plausible explanation for this irregularity is the beam reflection caused by the laser head or laser fiber, particularly as there was no back reflection protective mirror or glass for the multi-laser head. This suggests that reflected laser beams likely disrupted the measurement process. Consequently, for all calculations and assumptions, the width of the laser spot was taken as 72 μm.

During the experiment, the optical output power and multi-laser head loss of the laser were measured using an optical power meter (Thorlabs PM100D-S142C). The laser was measured at different power settings (0.5, 1.5, 2.5, 3.5 Amps), and it was found that the average maximum optical output per laser was 4.2 W. The power losses through
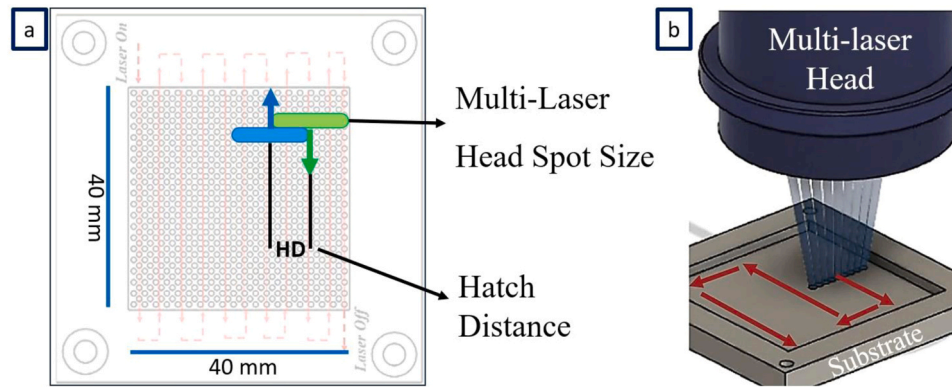
Fig. 4. (a) Visual Representation of the Employed Substrate Highlighting DAM Scanning Strategy, (b) Three-Dimensional Illustration of In-Situ DAM Process with Detailed Scanning Approach.

the multi-laser head were calculated to be around 16.9%. A laser power of 4 W was consistently applied during the experiment to avoid damaging the diode lasers themselves while using their maximum power (4.2 W).

2.1.2. System operating procedures

The multi-laser head was connected to a gantry movement system. The 316 L stainless steel with a dimension of 66 mm × 66 mm was used, and a central area of 40 mm × 40 mm was drilled with shallow holes to provide good bonding between substrate and specimens (Fig. 4-a). A silicone-based wiper was used to spread powder onto the substrate to enhance the spreadability (Capozzi et al., 2022). The build chamber was vacuumed till it reached −0.1 bar, and then argon gas was purged until the oxygen content dropped below 0.09% (measured by a Crowcon oxygen sensor embedded inside the build chamber). Then, argon gas was continuously purged just above the powder bed throughout the experiment to supplement the environment without disturbing or causing the raw powders to scatter. This circulation system protected the multi-laser head (because the focal distance is 60 mm ± 3 mm) from fumes and prevented material oxidation, akin to Direct Energy Deposition (DED) systems (Gong et al., 2022). One scanning strategy was used during all processing, which overlapped multiple tracks (Fig. 4) where the lasers were perpendicular to the scanning direction. During the scanning process, the multi-laser head remained in a fixed orientation, neither tilting nor rotating. The lasers were continuously active throughout the experiments, leading to the formation of high energy density sections at the locations where the multi-laser head is parallel to the scanning direction when crossing the next track with a designated hatch distance. Consequently, in top surface or cross-sectional examinations, areas 1 mm from the edge were disregarded. No additional heating sources were employed, including neither optical preheating nor powder bed heating, and studies were conducted at 20 °C laboratory temperature.

However, this new system's limitations can be stated as scanning speed range, cooling system, oxygen exposure, pre-heating, and current productivity rate. The scanning speed of the multi-laser head is in a range of 10–1000 mm/min (0.17 to 16.7 mm/s) due to the gantry system. Enhancements could involve adding a galvanometer scanner or a robotic arm, which enables laser head tilting and rotating. Secondly, the cooling system could be extended and upgraded to support up to 50 lasers (currently nine). While the DAM system's design minimizes oxygen exposure, the possibility of O_2 ingress during argon circulation cannot be entirely discounted. This could potentially lead to oxidation of the powder bed or built samples. Preheating the powder bed might offer a solution to interlayer fusion concerns, but it introduces the potential for heat-related damage to the closely positioned multi-laser head due to its focal length to the build plate. The highest density parameters of this study indicated that this current system's productivity rate is around 0.104 cm³/hr with nine lasers. Productivity can be increased by increasing the number of lasers, which would create wider melt pools and reduce the number of scans per layer, by increasing scanning speed with more powerful lasers, or by using preheating techniques with 2D laser arrays. Furthermore, the samples produced using DAM exhibited α + β structures, suggesting that this can eliminate the need for additional heat treatment, depending on the application.

2.2. Material specifications

The feedstock used in this study was Ti-6Al-4 V Grade 23 suitable for LPBF produced by gas atomization by Carpenter Additive. The particle size distribution of this material was 15–45 μm (90%), with most of the particles possessing a spherical shape (Additive, 2024). Additional specifications for this material are provided in Table 1.

2.3. Design of experiment

In this entire research, scanning speed is denoted as SS, hatch distance as HD, layer height as LH, and E_0^* is the normalized energy density value. Sample coding was based on references where parameter optimization involved adjusting E_0^*, impacting all parameters. This approach was chosen for clarity and ease of comparing different parameters under a unified code. For example, $100SS600HD70LH8E_0^*$ refers to a scanning speed of 100 mm/min, a hatch distance of 600 μm, a

Table 1
Detailed Specifications of Ti6Al4V Grade 23 Alloy.

Chemical Composition (Additive, 2024)									
Element	Ti	Al	V	Fe	O	C	N	H	Y
wt%	Balance	5.5-6.5	3.5-4.5	0.25	0.13	0.08	0.03	0.0125	0.005

Physical Properties at 1604 °C		units							
Specific Heat Capacity (C_p) (Additive, 2024)	0.5263	J/g°C
Melting Temperature (T_m) (Additive, 2024)	1604	°C
Material Density (ρ) (Additive, 2024)	4430	kg/m³
Thermal Diffusivity (α) (Alsaddah et al., 2022)	6.7×10^{-6}	m²/s
Absorptivity at 450 nm (A) (Alsaddah et al., 2021)	72	%

Table 2
Overview of Testing Parameters Used in the Experimentation.

Expanded Single Track Parameters (1)				Narrowed Single Track Parameters (2)			
LH	1000	μm		LH	1000	μm	
SS	50, 100-1000	mm/min	100 inc.	SS	20-90	mm/min	10 inc.
Size	20	mm		Size	20	mm	
Single Layer Parameters (3)				**Multi-Layer Parameters (4)**			
LH	400	μm		Area	5 × 5	mm^2	
SS	50, 75	mm/min		E_0*	1-25		
HD	300-1200	μm	100 inc.	LH	400,200,100	μm	
Size	5 × 6	mm^2		#L	20	Layers	

was used in Scanning Electron (SE, a.k.a. default) and Backscattering Electron (BSE) modes to take images of the surface and reveal the microstructure, respectively. Alicona Infinite Focus was used to measure surface roughness (R_a), with average R_a values obtained from five measurements with different line patterns (with the embedded Eq. (4) in the Alicona Infinite Focus Software, where $Z(x)$ is the profile height function, and L is the evaluation length). Images were processed using ImageJ software. Finally, Vickers hardness tests were carried out using a 500 g load with a dwell time of 15 s via Mitutoyo Indenter from the middle sections of the samples. The X-ray Diffraction (XRD) process was conducted with PANalytical Aeris with the start angle set to 30° and ending at 80° with a step size of 0.022° with a 10-minute rotating scan (2θ). To quantify the frequency of spattering, a chronometer was used, and the measurements were recorded per minute.

$$R_a = (\frac{1}{L}) \int_0^L |Z(x)|dx \qquad (4)$$

3. Results and discussion

3.1. Cooling rate vs E_0*

First, it is necessary to investigate the importance of cooling rate (CR) to understand its effect on samples and parameters with this bespoke DAM system. A high energy density can be created at slow SS, short HD, or a thin LH. Thus, a higher E_0* creates lower cooling rates for almost all the parameter conditions. The influence of SS, HD, LH, and, therefore, E_0*on CR is shown in Fig. 5. The correlation between CR and E_0* can be ascribed to the heat-affected zones (HAZ) resulting from the pre-heating of adjacent unmelted powder during in-situ melting of a single-track.

With an increase in the number of passes of the laser beam (short HD or high number of overlaps) within a processing layer (in situ), the temperature of neighboring powders gradually rises throughout the process. This reduction in the temperature gradient (ΔT) during melting for each subsequent pass results in a higher overall temperature for the completed tracks compared to the high HD version of a sample. This, in turn, prolongs the time during solidification and, therefore, might affect the phase transition. This low CR can also be explained with the SS and LH in the same way. Slow SS affects the adjacent raw powders' temperature in the same way as HD, and thin LH means less material to melt and fuse the layer beneath.
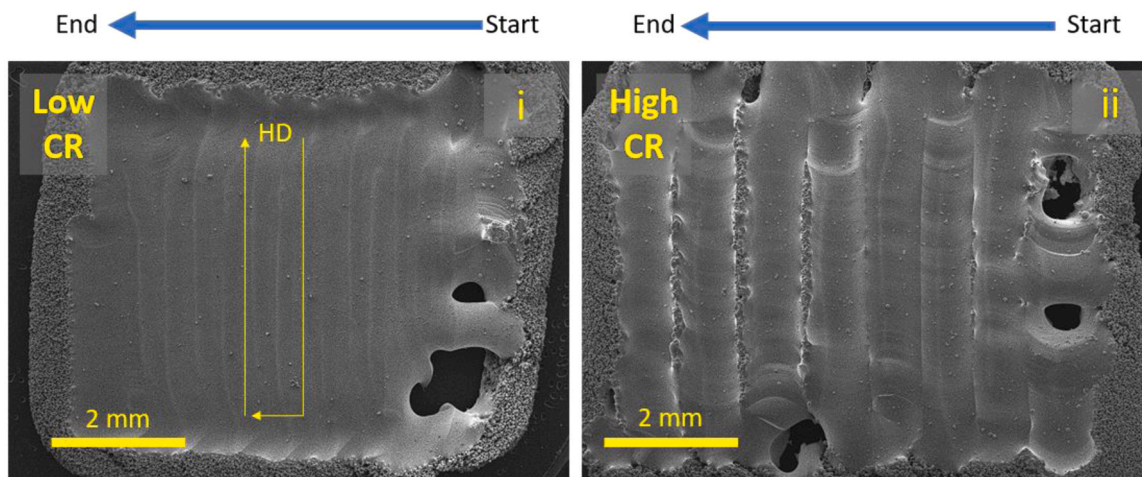
layer height of 70 μm, and E_0* will be equal to 8.

Table 2 outlines the parameters used in this research, with initial selections based on similar setup studies and their findings by (Alsaddah et al., 2021) and (Alsaddah et al., 2022). Initial wide-range single-track studies identified the optimal E_0* parameter region for Ti64 processing (parameters listed in Table 2–1). In contrast to conventional LPBF, which typically uses an LH of about 40 μm (Shipley et al., 2018), this study first used thicker layers to determine the penetration depth of the laser to powder bed. 1000 μm LH was selected to facilitate sample removal without damage, allowing for cross-sectional analysis of penetration and other phenomena, crucial in this novel study with low-power, adjacent multi-lasers where outcomes were uncertain. The parameter range was refined and narrowed for single-track melting (parameters listed in Tables 2–2), and based on the single-track results, a few parameters were chosen for single-layer studies at 400 μm LH (parameters listed in Tables 2–3). LH of 400 μm was determined through a small preliminary experiment. The LH was dropped from 1000 μm gradually till the penetration of the laser reached optimal substrate adhesion and damage-free removal. Finally, an E_0* range for multi-layer fabrication was established (parameters listed in Table 2–4) based on these optimal parameters found in Tables 2–1, 2, and 3. For the multi-layer study, 20 layers were processed after 30 layers to eliminate surface waviness caused by the holed substrate. For the purpose of consistency testing, three samples were fabricated for each parameter set.

The degree of melting and densification achieved was measured through cross-sectional imaging with Light Optical Microscopes (LOM) (samples were hot mounted and analyzed with a Nikon LOM). Sample preparation included grinding from 320 grit to 4000 grit, followed by a polishing stage using a 0.06 μm colloidal silica with 10% H_2O_2 solution. Oxford Instruments Tescan Vega 3 Scanning Electron Microscopy (SEM)

Fig. 5. Assessment of Cooling Rate (CR) Effects via Top Surface SEM Imaging: Parameter Samples (i) 50SS400HD100LH23E_0* and (ii) 75SS800HD400LH2E_0*.
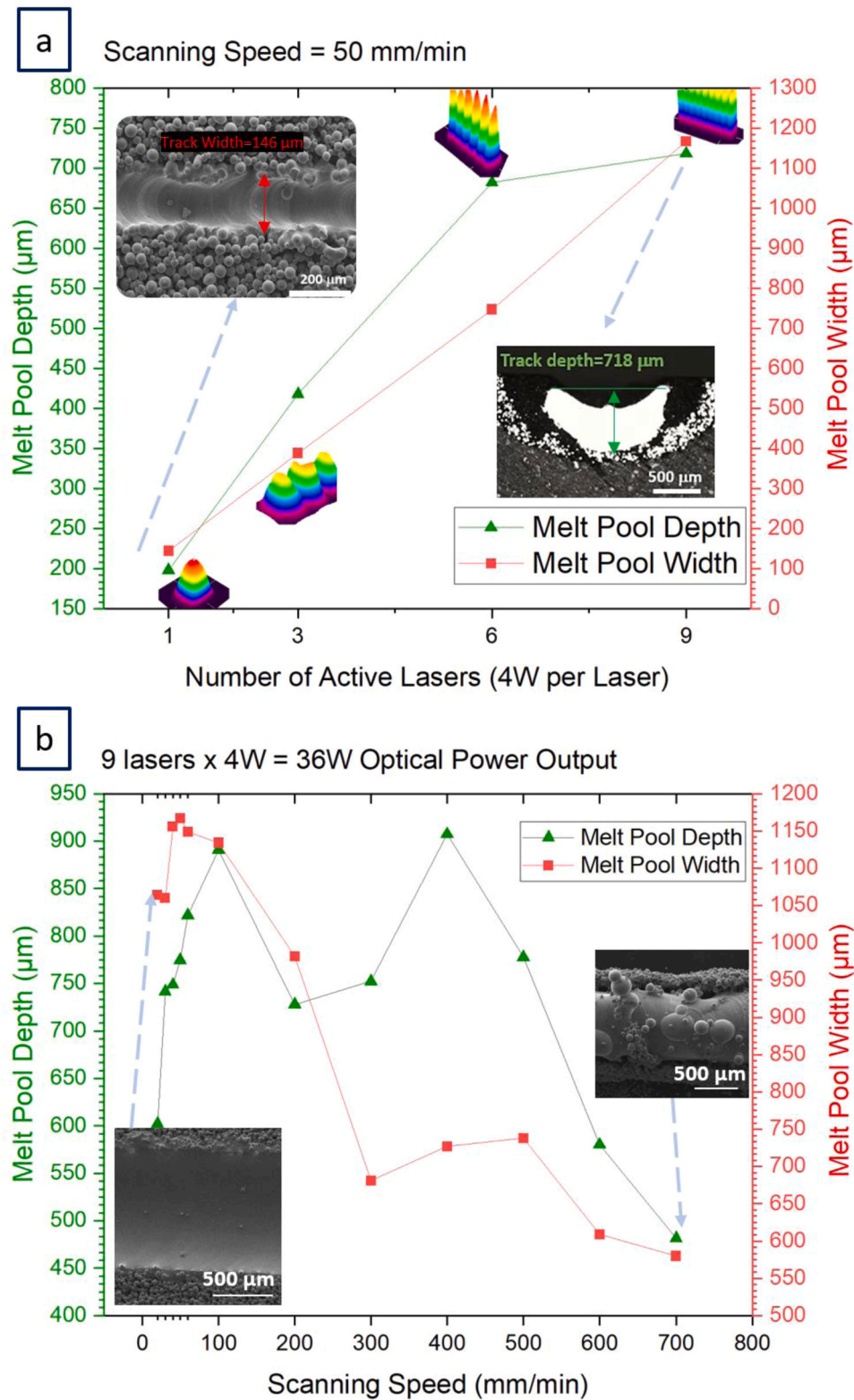
Fig. 6. Single Track Graphs Depicting Melt Pool Width and Depth: (a) Correlation with Number of Active Lasers, (b) Correlation with Scanning Speed.

3.2. Preliminary parameter studies

3.2.1. Single track studies

This section explored how the number of diode lasers affects melt pool width and depth, seeking to understand the variation in melt pool dimensions with the use of consecutive active lasers and their parameters.

Firstly, LH was set at 1000 μm, and SS was set at 50 mm/min for a single-track length of 20 mm for a number of laser impacts on the melt pool with the study, in accordance with prior research (Alsaddah et al., 2021; Alsaddah et al., 2022) methodologies. Examination of data derived from the beam profilometer (indicating FWHM beam dimensions of 52 μm, 215 μm, 430 μm, and 659 μm for laser groups employing 1, 3, 6, and 9 lasers, respectively) and the results of these

Table 3

Findings from Single-Track Parameter Tests (S2S – Sticked to Substrate).

Parameters	Observations / Defects					
Speed (mm/min)	HAZ (µm)	Cracks	Spatter (particle (s))	Balling	Substrate Penetration	Track Continuity
20	≈ 2000	Major	0-2	No	S2S	Yes
30	≈ 1000	Minor	0-3	No	S2S	Yes
40	≈ 500	No	1-3	No	S2S	Yes
50	≈ 450	No	1-4	No	S2S	Yes
60	≈ 400	No	2-5	No	S2S	Yes
70	≈ 300	No	2-5	No	S2S	Yes
80-200	300-200	No	10-30	Yes	Half S2S	Yes
300-500	≈ 200	No	30 +	Yes	Separated	Yes
600-1000	N/A	N/A	High (50 +)	Yes	Separated	No

single-track studies unveiled an expected observation: the melt pool width was approximately 75% greater than the number of active laser irradiated area within these four distinct laser groups. Furthermore, both the melt pool's width and depth demonstrated a corresponding increase (as depicted in Fig. 6-a). However, it is important to note that the melt pool depth appeared to have a limit to its penetration depth, even as the number of lasers increased (and therefore, the laser-irradiated width of the melt area increased). This can be explained by the fact that there was no significant change in the energy input per unit area on the powder bed, whether a single laser was used or a configuration using all nine lasers.

In Fig. 6-b, a parameter study was conducted with nine lasers (36 W) to observe the effect of varying scanning speed on melt pool width and depth with Table 2–1 and Tables 2–2 data sets. The study reveals an upward trend from 20 to 80 mm/min SS for melt pool width, but this trend continues towards 100 mm/min SS for melt pool depth. At the low SS range (20 to 100 mm/min), too much heat accumulates at the focal point, resulting in an extremely high temperature. Without preheating the powder bed, there is a significant temperature gradient between the melting point and the surrounding powders, causing rapid heat conduction towards the powders and resulting in the melting of a larger area to achieve larger melt pools. The cross-sectional dimensions of the samples tend to become spherical at a speed of 300–500 mm/min SS. It should be noted that the measurements were taken from the top surface of the solidified track to the last solidified section of penetration. The top surface peak point of the solidified tracks was higher than that of the slow SS tracks. The sphericalness increases in depth due to the balling phenomena on the graph between the 300–500 mm/min SS region. That is why there appeared to be an increase in depth in the graph. After reaching a speed of 500 mm/min, both the dimensions of the melt pool decreased, and discontinuous tracks were observed due to the high sintering rate at high speed. It can be generally concluded that an increase in SS (after 100 mm/min) results in a decrease in both the depth and width of the melt pool.
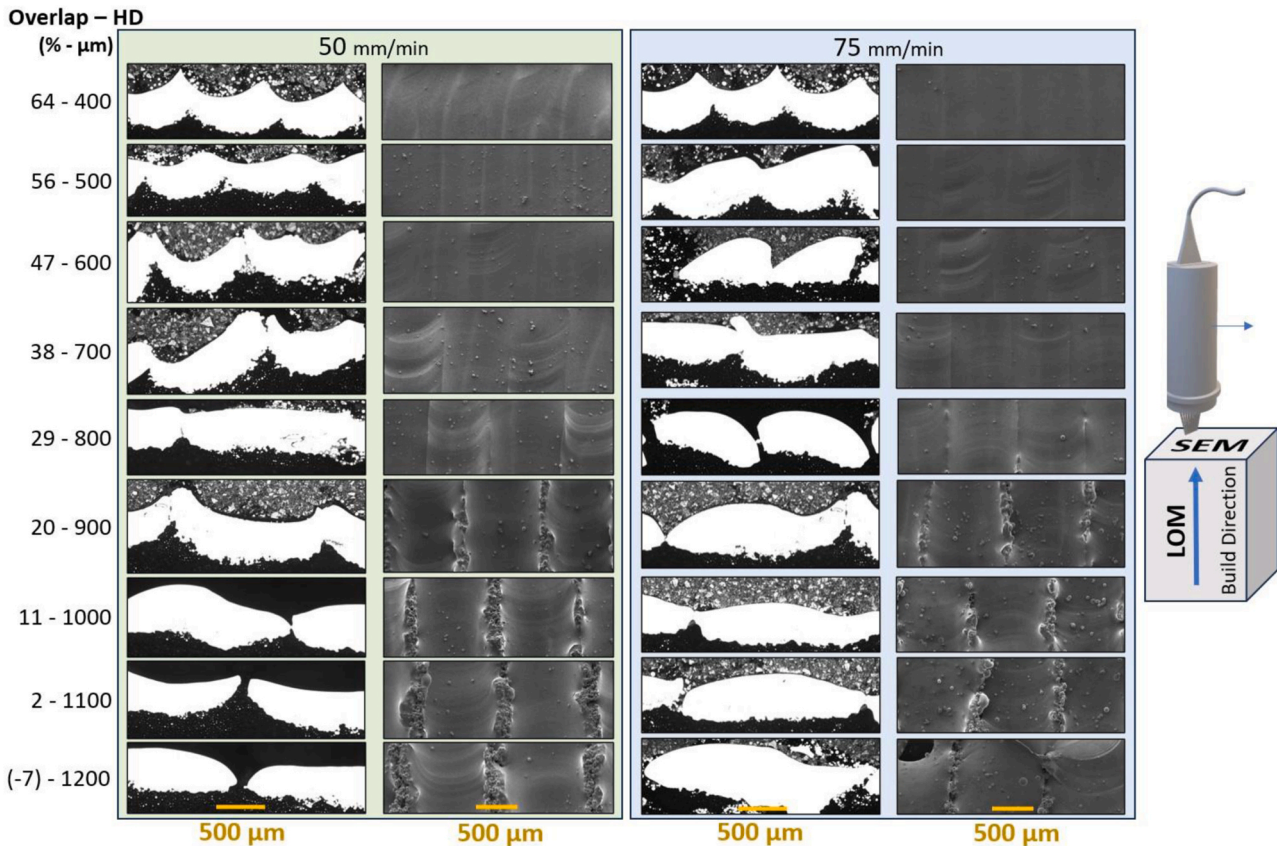

Fig. 7. Cross-Sectioned LOM and Top Surface SEM Images of Hatch Distance Study Samples: 50 mm/min Column (Green) and 75 mm/min Column (Blue), with Yellow Bars Indicating 500 µm Scale for Each Column.
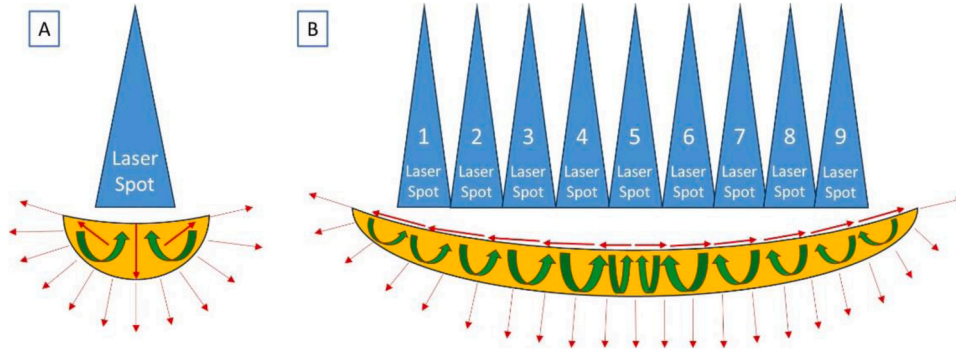
Fig. 8. Illustration of the Crescent Effect: Depicting Marangoni Flow with Green Arrows and Heat Transfer with Red Arrows in (A) Single Laser and (B) Multi-Laser Processing.

During the investigation of single-track processing, the first assessment examined various physical characteristics within the samples. These assessments included an evaluation of the heat-affected zone (HAZ) surrounding the sample, the presence of cracks, the occurrence of spattering effects, the existence of balling phenomena, the degree of substrate penetration, and the assessment of the continuity of the tracked path. A detailed compilation containing information regarding these defects and observations has been provided in Table 3. Single tracks with a scanning speed between 40 and 80 mm/min resulted in the smoothest surface finish, amongst others. The observation of spattering decreased significantly when SS was below 80 mm/min compared to higher speeds. In addition, the powder can still be melted even at a speed of 90 to 500 mm/min, yet with defects. The HAZ is considerably larger compared to single laser LPBF systems due to the inherently slow SS (Alsaddah et al., 2022). The HAZ was measured from the last solidified section of the tracks towards the end of sintering until reaching the raw powder. As a result, the HAZ decreased with an increase in SS because the energy applied per unit area at a specific time decreased. In practice, the HAZ remained relatively linear beyond an SS of 300 mm/min. In particular, at SS above 600 mm/min, the powder merely sintered, eliminating any clear reference point to begin measuring the HAZ. It is worth noting that when the SS is limited to values as low as 20 or 50 mm/min, spattering is either minimal or occurs in low amounts, typically involving fewer than five ejected particles per second. This phenomenon presents a stark contrast to industrial LPBF systems, where spattering tends to be more prominent with increased speed (Young et al., 2020). Cracks likely occurred due to a high cooling rate. The degree of substrate penetration was judged by the removability of the tracks from the substrate.

3.2.2. Single layer studies

The investigation centered on determining the optimal overlap value to achieve the highest attainable density while upholding surface quality. Three crucial factors guided this assessment: cross-sectional analysis and the average surface roughness (R_a) of the top surface. The powder was applied at a thickness of 400 μm as outlined in the methodology. Overlap percentage was calculated (Eq. (5)) using the average melt pool width (1078 μm) at 50 and 75 mm/min SS, with negative values indicating no overlap and positive values denoting overlap (Tables 2–3).

$$Overlap\ Percentage\ (\%) = \frac{(Melt\ Pool\ Width - Hatch\ Distance)}{Melt\ Pool\ Width} * 100$$

(5)

Fig. 7 illustrates the HD effect on the sample. Top surface views consistently exhibited nearly full density up to 800 μm HD. However, when examining the cross-sectional view, it becomes evident that full
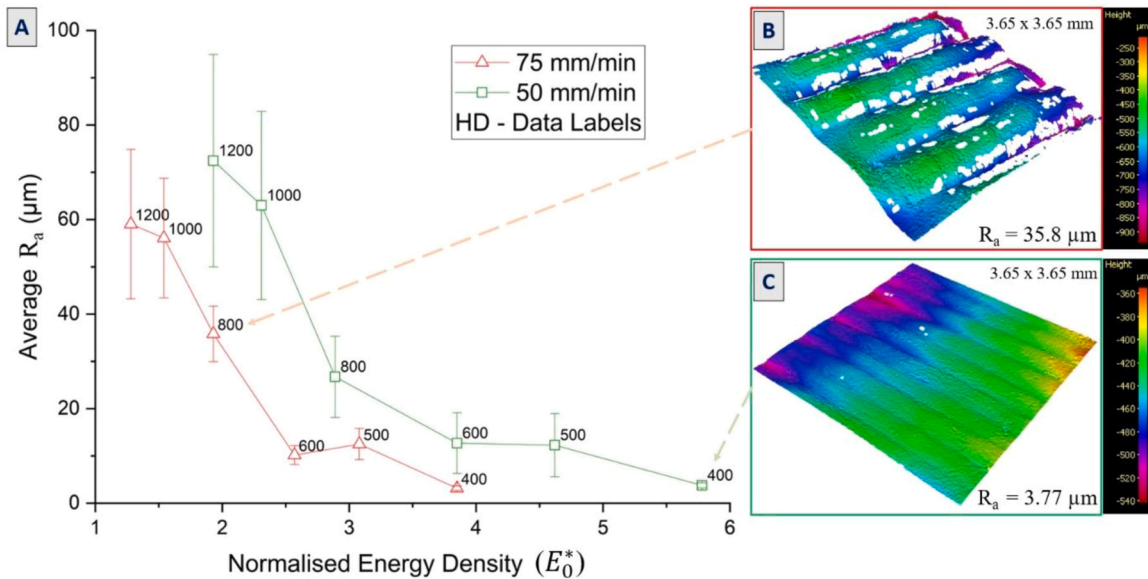

Fig. 9. (A) Graph of the Correlation Between Surface Roughness (R_a) and Normalized Energy Density (E_0^*) Using 3D Light Spectrometry Images with Hatch Distance (HD) Labels at (B) 75SS800HD and (C) 50SS400HD.
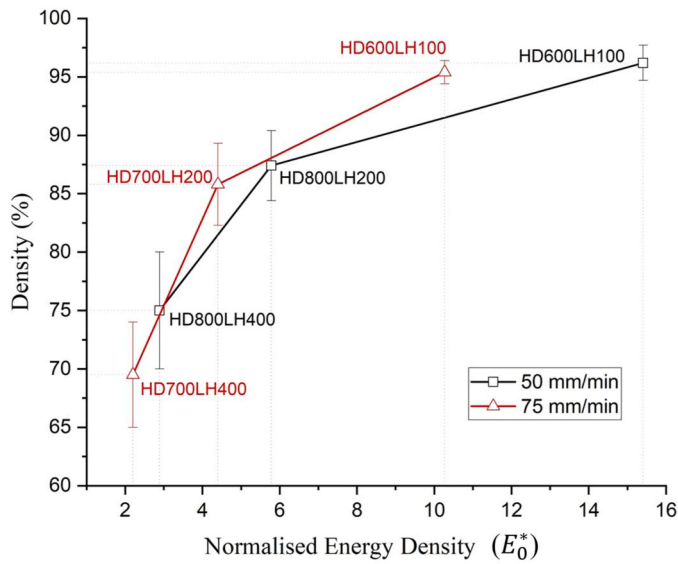
Fig. 10. Analysis of the Correlation Between Sample Density and Normalized Energy Density (E_0^*) Across Various Parameter Sets.

bonding was only achieved at 400 μm HD and 500 μm HD. Beyond 900 μm HD, at both scanning speeds, sintered powders began to accumulate between the tracks. Samples with a 300 μm HD consistently shattered or cracked during cross-sectioning in all experiments, likely due to a substantial thermal gradient caused by the lack of substrate heating. Therefore, the study did not continue to investigate 200 μm HD and 100 μm HD.

The tracks exhibited a crescent shape, with the curvature becoming more pronounced towards the edges as the HD decreased. This was due to the lasers being perpendicular to the scanning direction. This phenomenon, herein referred to as "the crescent effect" (illustrated in Fig. 8 and shown in Fig. 11), is anticipated to have implications for the density of multi-layered samples. This phenomenon could be attributed to Marangoni flow (Khairallah et al., 2016), heat transfer dynamics (Zhang et al., 2018), and recoil pressure (Zhang et al., 2018). This wider melt pool exhibits a temperature distribution like a crescent moon, with a hotter center and cooler edges. This is driven by Marangoni flow, where surface tension differences due to temperature variations pull the liquid towards the hotter center. Moreover, the melt pool near the first laser experiences heat transfer towards the cool powder bed and substrate on the bottom side. On the other hand, the melt pool bottom of the fifth laser, surrounded by high temperatures, transfers its heat primarily toward the cooler substrate. Furthermore, the recoil pressure contributes
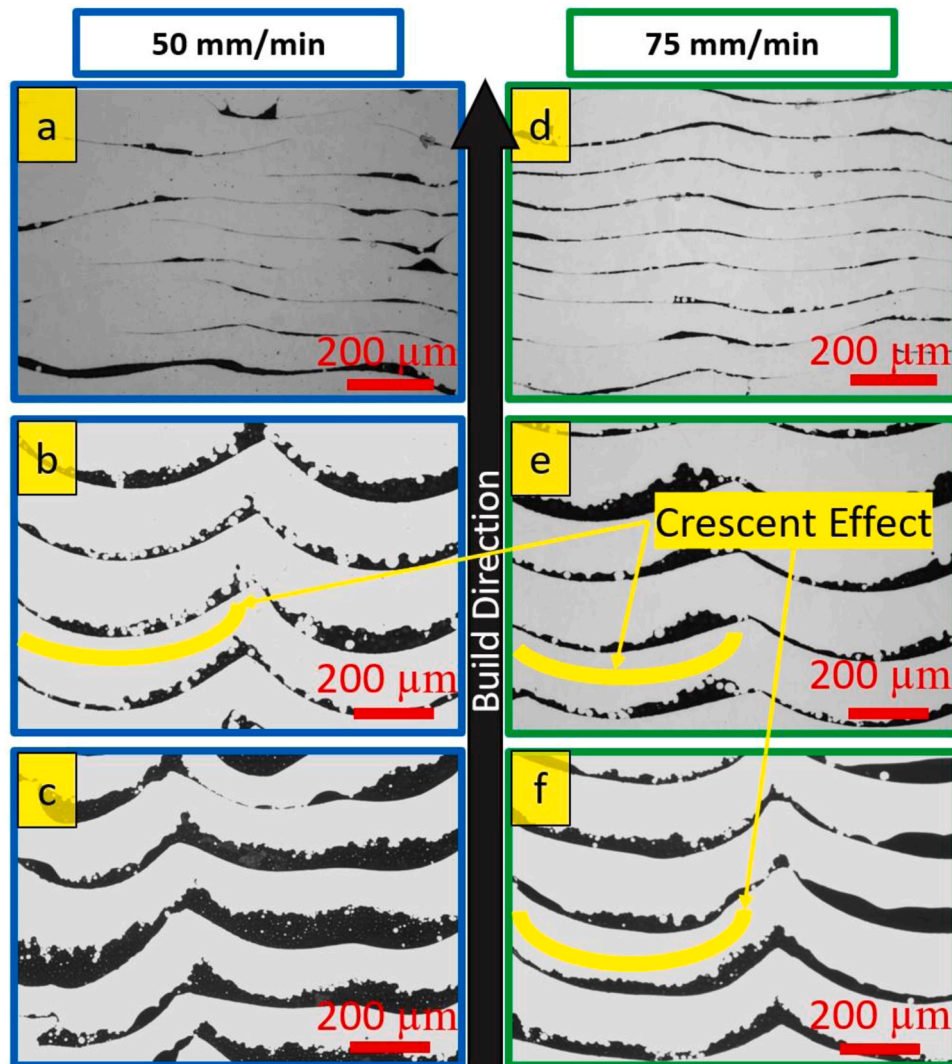

Fig. 11. LOM Cross-Sectioned Images Displaying Various Parameter Sets, Including Illustrations Explaining the 'Crescent Effect' (where (a) 600HD100LH, (b) 800HD200LH, (c) 800HD400LH, (d) 600HD100LH, (e) 800HD200LH, (f) 800HD400LH). (Black sections are porosity/air gap/lack of fusion).
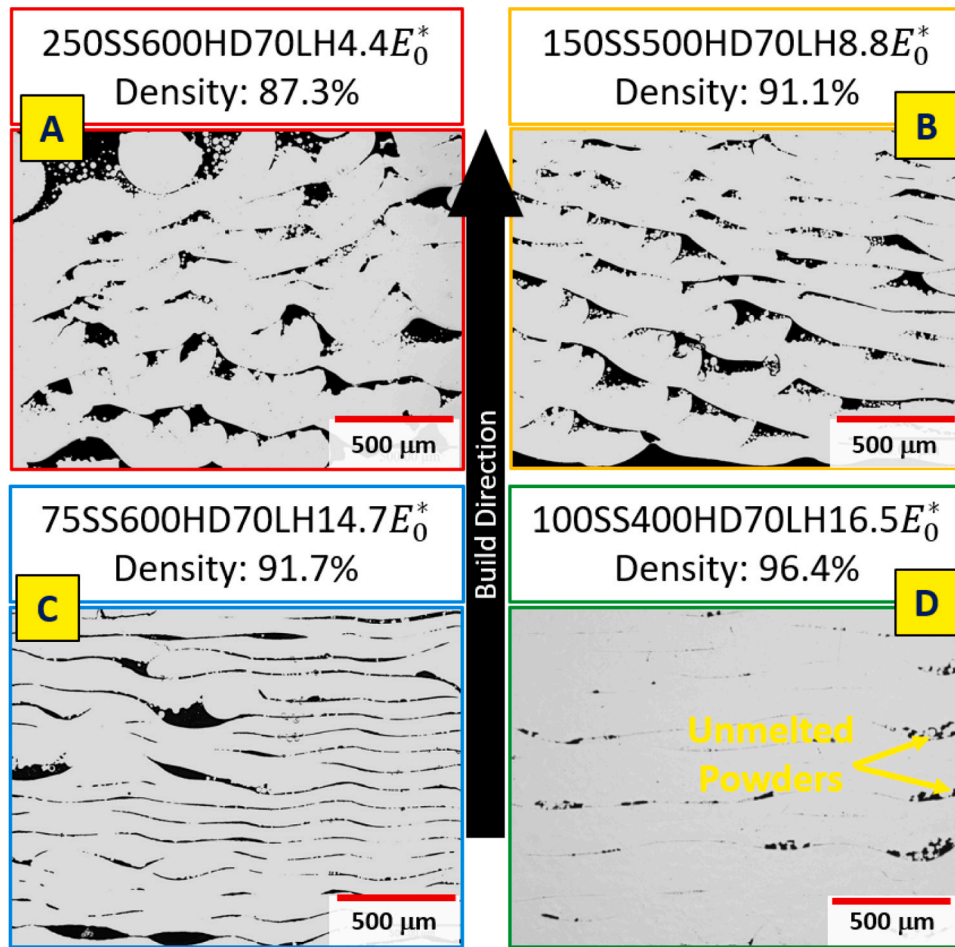
Fig. 12. Visual Analysis of Densification via Cross-Sectioned Images in Normalized Energy Density (E_0^*) Study. (Black sections are porosity).

to the crescent shape by pushing molten metal downwards, potentially impeding downward heat flow near the center where the pressure is highest. These combined factors shape the melt pool dynamics, concentrating heat at the center and sharpening the curvature at the edges, reinforcing the crescent shape.

In pursuit of enhancing uniformity in the layering process during multilayer fabrication, an investigation into surface roughness (R_a) measurements was carried out to elucidate the relationship between R_a and E_0^* while limiting the influencing factor to only SS and HD (as depicted in Fig. 9-A). The HD analysis suggests that rougher surfaces might lead to non-uniform layer heights, potentially causing uneven energy density distribution across the layer due to variations within the layer from the crescent effect. Moreover, the study showed a decrease in R_a with a decrease in SS and, therefore, increased energy density. Additionally, an inverse correlation between HD and SS with surface roughness was identified, which could be divided into two distinct sections. To categorize the sections for the study's purposes, the first section could be identified when HD exceeded 800 μm, while the second section could be identified when HD fell below 800 μm. The first section pertained to the discontinuities observed between tracks, primarily attributed to an insufficient number of lasers (or inadequate overlap) or a high CR, which resulted in a reduced energy density, thereby promoting sintering of the material rather than complete melting (Fig. 9-B). The second section came into play when tracks fused with prior tracks. In this case, a shorter HD assumed lowered the CR and lessened the crescent effect in the region. It is possible that the edge of the previous track was partially remelted and resolidified, therefore reducing the height of the peaks. (Fig. 9-C).

3.3. Multilayer studies based on E_0^*

3.3.1. Densification studies

In single-layer fabrication, the optimal HD parameters were below 800 μm, resulting in a larger surface melting between tracks, according to Fig. 7 and the roughness study in Fig. 9. The SS was set at 50 mm/min and 75 mm/min, with 75 mm/min being the upper limit based on the results of the single-track study. For SS and HD parameters related to the SS, groups with similar E_0^* values were selected. The LH study began at 800 μm and involved the lower half of each group until 100 μm, as shown with all other parameters in Fig. 10 from Table 2–4. The 800 μm LH layer is not displayed in the graph because it delaminated due to insufficient fusion.

A couple of samples in Fig. 10 are shown in Fig. 11. The modification of HD values to 600 μm in Fig. 10 was due to inconsistent E_0^* within a single layer (Fig. 11-b-c-e-f), attributed to the crescent effect (Section 3.2.2). Consequently, HD values were reduced value level at a time (from 800 to 700 and then to 600) to ensure consistency. According to Fig. 10, with a short HD of 600 μm and low LH of 100 μm, it is possible for the samples to reach high-density regions (>95%) and display a connection with the solidified layer beneath. Furthermore, it has been discovered that a high E_0^*, achieved by decreasing the LH, increases density.

Moreover, the LH was reduced to 70 μm, an optimal LH reported in a previous study (Alsaddah et al., 2022), and four distinct parameters were chosen in the E_0^* region, which is assumed to be within the upper and lower limits, to establish the boundary conditions of the high densification section for multi-layer study only. This section is between E_0^*=4.4 and E_0^*=16.5 (derived from (Alsaddah et al., 2021) and
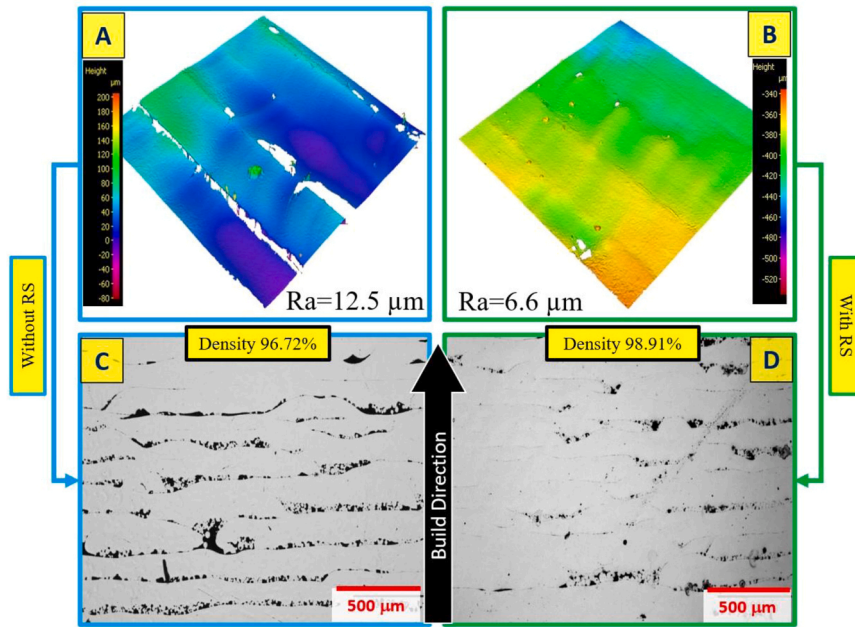
Fig. 13. Impact of Rescanning (RS) on Top Surface Roughness (R_a) and Density: (a) and (c)without RS Strategy, (b) and (d) with RS Strategy, (a) and (b) Represents R_a, (c) and (d) represents LOM Images. (Parameters: 100SS400HD70LH for both samples, with or without RS250SS400HD).

(Alsaddah et al., 2022)). The cross-sectional images are shown in Fig. 12. According to these images, the density increases with the E_0^* (from Fig. 12-A to Fig. 12-D). Furthermore, A and C in Fig. 12 are comparable in terms of SS, as all other parameters remained constant. Consequently, the slower process speed results in higher densification. It can be concluded that only (Fig. 12-D), which was above the E_0^*=16 region, has sufficient energy to achieve high-density (>95%) parts. Nonetheless, higher energy input is necessary to attain near-full dense samples by reducing the LH, as it was observed that some unmelted powders (Fig. 12-D) were present between the layers, which led to porosity and lack of fusion defects. Hence, a nearly full-density sample has not been obtained yet.

3.3.2. Rescanning effect on densification and parameter map

A lower energy density strategy was implemented in rescanning (RS) to achieve higher density in DAM parts. According to (Liang et al., 2022) and (Miao et al., 2020), this strategy results in smoother top surfaces. The investigation used parameters 100SS400HD70LH (Fig. 12-D), which has yielded the highest density observed thus far. The RS process was conducted at a speed of 250 mm/min. The chosen speed was determined based on trials at five different speeds: 100, 250, 500, 750, and 1000 mm/min, all under the same layer processing parameters

(100SS400HD). Among these, the 250 mm/min SS yielded the lowest R_a. It's notable that at 100 mm/min, the samples showed slight warping, often causing the wiper to dislodge them from the substrate in subsequent layers. From 250 mm/min upwards, R_a decreased from 10.6 μm to 6.6 μm, with the lowest R_a observed at 250 mm/min and the highest at 1000 mm/min. The RS process was initiated in reverse once the powder melting within a layer was complete, stopping at the initial melting start point and maintaining the lasers active during the entire layer processing.

RS significantly decreased surface roughness by almost 50% (Fig. 13-A-B) and increased sample density by 2% (Fig. 13-C-D). A higher E_0^* parameter was required to achieve more significant densification. Consequently, LH was reduced to 60 μm while maintaining the same parameters (100SS400HD60LH, E_0^*=19.3) to ensure comparability of results with Fig. 13. Additionally, a slightly higher E_0^* parameter (E_0^*>20) was chosen. SS was lowered to 75 mm/min due to its ability to produce smooth and consistent tracks, and HD was set at 500 μm, resulting in an E_0^* of 20.5 for 75SS500HD60LH. Henceforth, all samples were fabricated using RS. According to Fig. 14, lowering the LH to 60 μm increased the density, increased the fusion between layers, and reduced the porosity compared to the 70 μm LH version. Moreover, the highest density was achieved with E_0^*= 20.5 parameters with the RS strategy
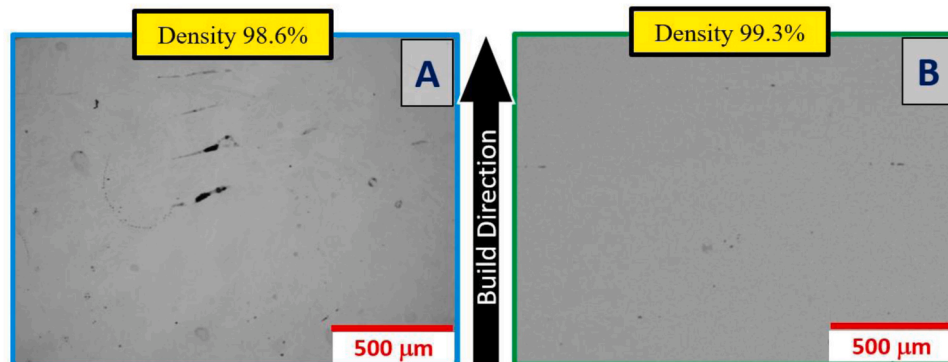

Fig. 14. LOM Images of 60 μm LH Samples Under Varying E_0^* Settings: (A) Parameters 100SS400HD60LH19.3E_0^*, (B) 75SS500HD60LH20.5E_0^*. (Black sections are porosity).
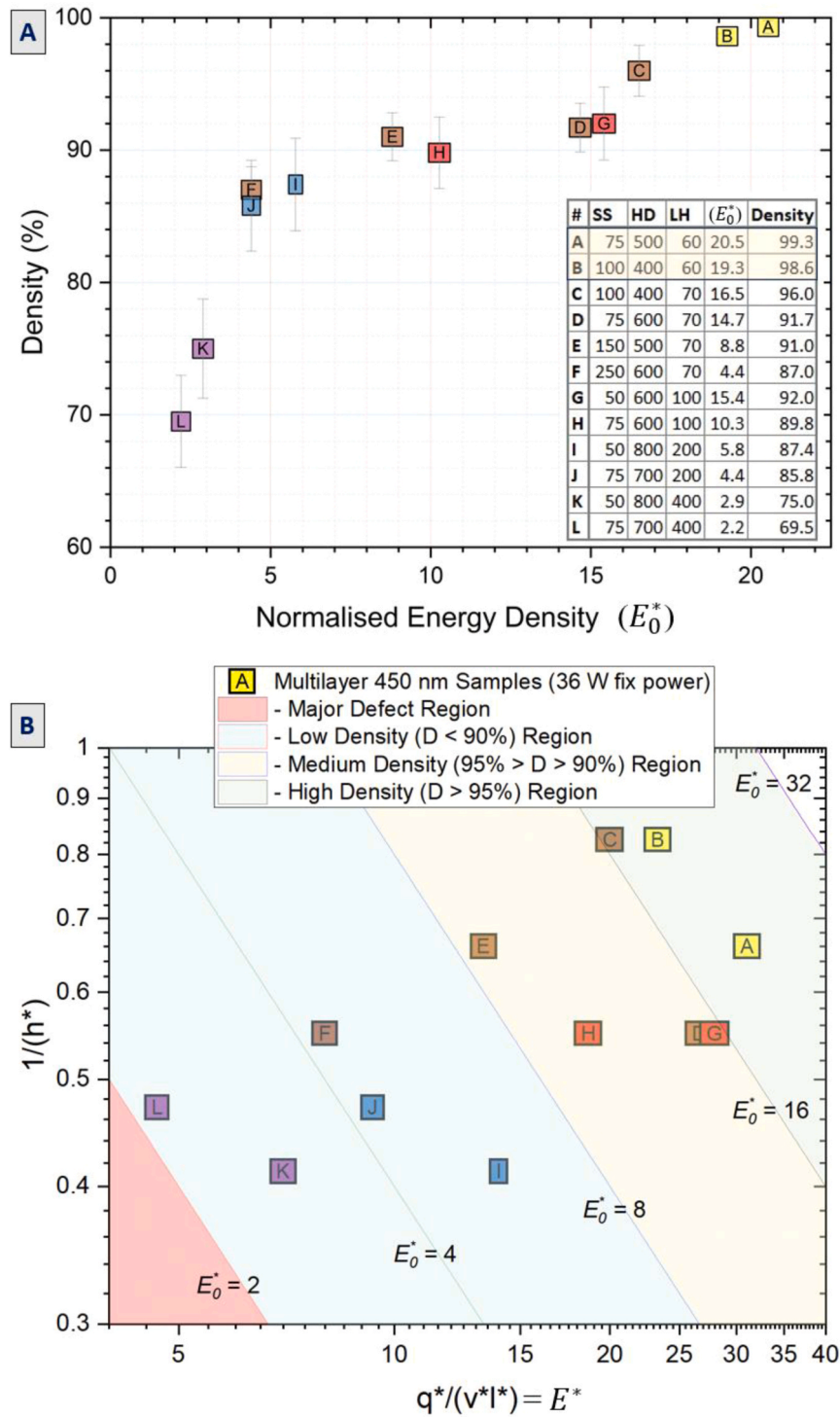
Fig. 15. (A) Overview of Densification Studies,(B) Revised E_0^* Colored Chart Reflecting Study Findings (Table in A Details Parameters, E_0^*, and Sample Densities; Rescanned Samples Highlighted in Yellow).

(Fig. 14-B).

To visually analyze the tested parameters, Fig. 15-A shows a density chart incorporating E_0^*.Utilizing data from this chart, a corresponding E_0^* chart was generated, color-coding the E_0 regions based on sample density, as illustrated in Fig. 15-B. These graphical representations serve the purpose of creating a parameter map that delineates the regions where densities exceed 95%. Based on the analysis outcomes, it can be stated that it is possible to achieve high-density samples in the DAM system by using nine 450 nm 4 W diode lasers without preheating, with

the condition of $E_0^* > 20.5$. In contrast, (Alsaddah et al., 2022) reported that ten 5 W 808 nm diode lasers arranged in arrays can achieve part densities of 98% and above when coupled with up to 300 °C powder bed heating module (Alsaddah et al., 2021). Therefore, it can be compared in one aspect that 450 nm diode lasers have the potential to be approximately 28% more efficient (in terms of power required) than their 808 nm counterparts in the DAM system. (50 W in 808 nm (Alsaddah et al., 2022) (higher than 95% density) versus 36 W in 450 nm (99.3%)) when disregarding the energy consumed for the RS. It's important to
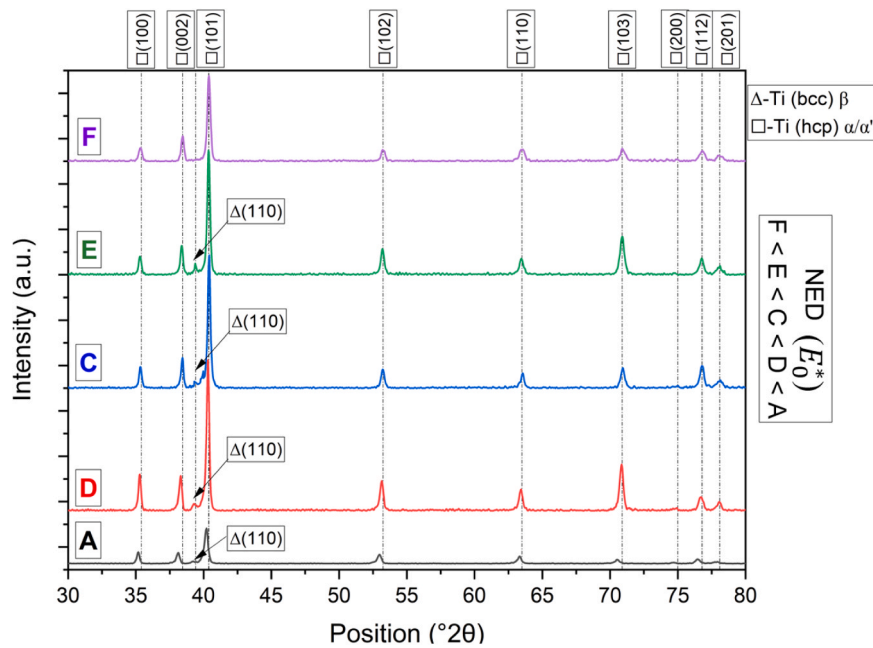
Fig. 16. XRD Data Analysis Corresponding to their Normalized Energy Density (NED) Values with sample F- 250SS600HD70LH, sample E- 150SS500HD70LH, sample C- 100SS400HD70LH, sample D- 75SS600HD70LH, sample A- 75SS500HD60LH parameters.

note that efficiency calculations warrant further scrutiny, especially given the different operational configurations, as the 808 nm system operates in arrays (comprising two arrays with five lasers each). Furthermore, in order to explore the region of excessive energy on the parameter map, it is necessary to either increase the number of lasers or replace a single laser's power output with something greater than 4 W or lower LH to less than 60 μm. These limitations led to the absence of an excessive energy area on the E_0^* parameter map compared to (Alsaddah et al., 2022).

3.4. Characterization

3.4.1. Phase determination

The purpose of XRD was to verify the existence of α'/α and β structures (Thijs et al., 2010). α and α' are Hexagonal Close Packed (HCP), and β phase is a Body-Centered Cubic (BCC) structure. This is the reason why variable peak locations are observed during XRD analyses (Owen, 2022). XRD patterns (Fig. 16) were obtained from 70 μm LH (C, D, E, F) data and the highest dense part (*A* with 60 μm LH) to investigate the influence of different CRs on phase formation based on E_0^*. For Ti64, if the CR exceeds the value of 410 °C/s, there will be a complete transformation into the martensite phase (α'), which originates from the primary β grains ($T_\alpha = 595$ °C, $T_\beta = 995$ °C) (Wu et al., 2016). ICDD PDF4 + cards (Powder Diffraction File) 04–020-7055 (Gates-Rector and B. T, 2019) for α and 00–044-1294 (Gates-Rector and Blanton, 2019) for β (as it cannot be detected at room temperature (Wu et al., 2016)) were used to identify phases.

According to Fig. 16, no β peaks were observed in the sample with the lowest E_0^* (F (E_0^*=4.4)) due to its rapid CR among other samples, which gives a similar trend to traditional LPBF results (Pathania et al., 2022). It can be concluded that if E_0^* is lower than 8, only α'/α peaks, and if it is higher than 8, β peaks will be observed for 450 nm DAM parts, supported by the findings of (Alsaddah et al., 2022) as they stated that with 600 °C/s CR, β peaks were observed. Furthermore, sample A showed a shift in the graph, although this shift did not pertain to one or a couple of peaks, as it affected all peaks. Therefore, it can be inferred that the height of the sample was the issue during the XRD procedure. However, a small shift within a single peak may occur due to microstrain, temperature changes, compositional variations, or lattice

imperfections, which can contribute to peak shifts in XRD patterns (Owen, 2022). Fig. 16 illustrates that with an increase in E_0^* (or a decrease in CRs from sample F to Sample A), the peaks become less intense. This reduction in peak intensity could be due to microstrains from dislocations, preventing the alloy's atoms from dissolving sufficiently (Xiao et al., 2020). This leads to increased residual stress, resulting in peak broadening instead of sharpening, indicative of smaller crystal grains (Owen, 2022). However, a more thorough study and analysis are needed to fully understand residual stress, either through conventional measurement techniques or high-temperature modes, to ascertain the exact cause of the decrease in peak intensity after a specific cooling rate.

3.4.2. Microstructure analyses

Sample A (99.3% dense with rescanned each layer (75SS500HD60LH)) was used to investigate the microstructure of 450 nm processes Ti64 material as other samples had severe porosity and lack of fusion defects. As shown in Fig. 16, α and β phases exist in Sample A. Therefore, SEM image analyses were undertaken with BSE mode to contrast α and β. Heavy elements such as Vanadium (V) and Iron (Fe) in Ti64 are the stabilizing elements of the β phase, and they can be seen as brighter lines and points under the BSE mode in SEM (Gaillard et al., 2023).

The microstructure along the vertical direction of the build exhibited significant variations across sections, as shown in Fig. 17-A1, A2, and A3. Rescanning may also influence the type of structure and grain length distribution due to extra heat energy applied to the material just after solidification (assuming it increases the solidification time). Notably, Section A3 displayed coarser lamellar type $\alpha + \beta$ and α' structures, resulting from slower CRs that led to minimal temperature differences between adjacent layers. This suggests a partially annealed state with fewer acicular α' structures, particularly in the lower portion of the specimen. This $\alpha + \beta$ occurrence is attributed to the increase in temperature of the bottom layer as subsequent layers are processed, leading to a decrease in the CR. In contrast, the grain sizes in section A1 demonstrated finer and more martensite α' sub-grains as they approached the build direction. Therefore, an increase in CR, which creates fewer acicular α' structures, occurs when it is getting closer to the top surface (Zhang et al., 2018). Additionally, the entire sample
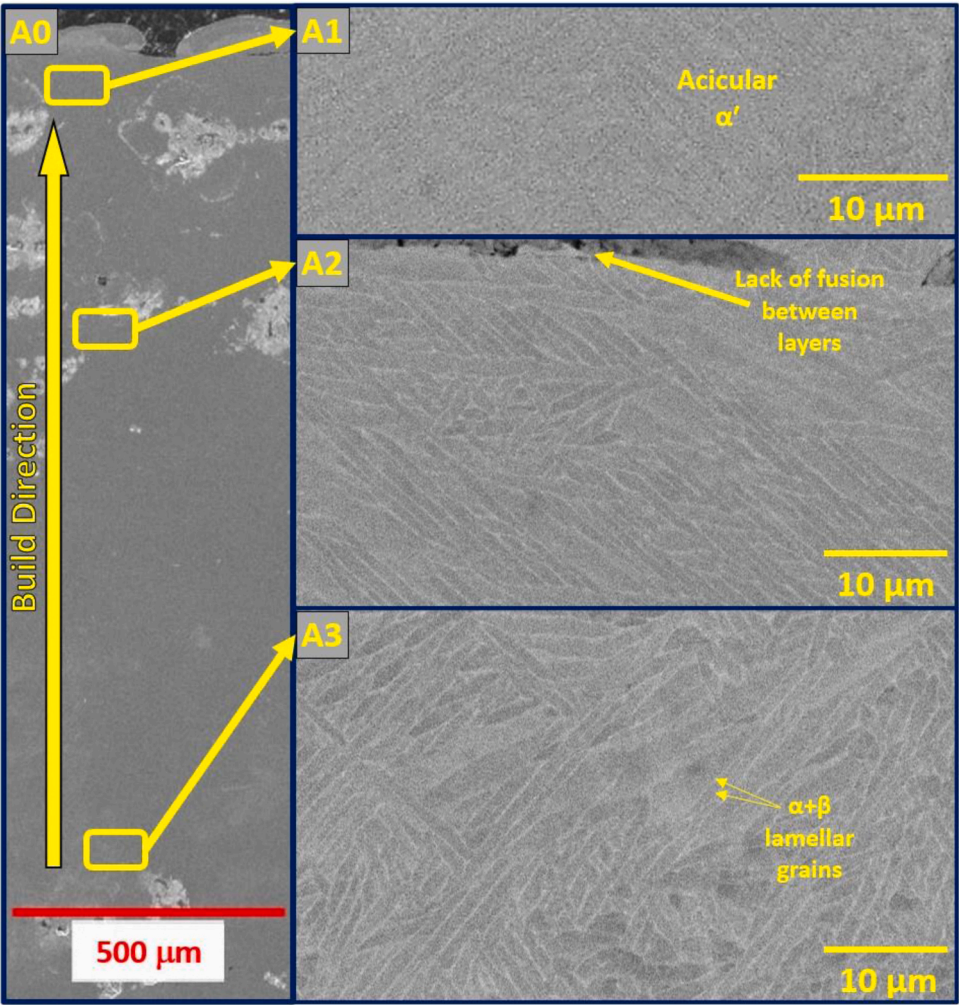
Fig. 17. SEM-BSE Microstructural Analysis of Sample A: (A0) General View at Lower Magnification, (A1) Top Surface Detail, (A2) Middle Section, (A3) Middle-Bottom Section (Etching Procedure was not Conducted).
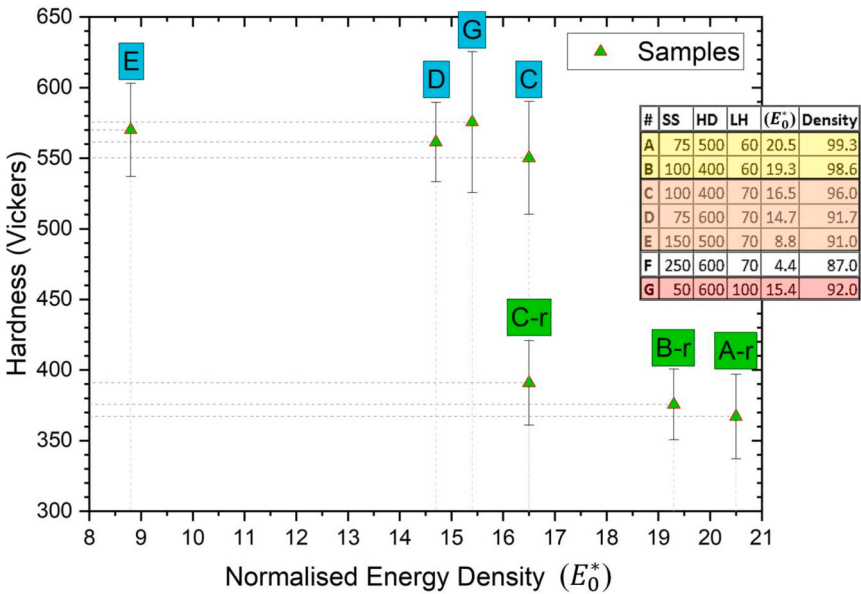

Fig. 18. Vickers Hardness Versus Normalized Energy Density (E_0^*) in High-Density Samples: Focus on Samples Above 90% Density, Including Rescanned Samples C-r, B-r and A-r.

generally displayed a basket-weave type microstructure, which was particularly evident in section A1. For a valid comparison of microstructures between traditional single laser LPBF-produced Ti64 and those produced using DAM, the processing conditions should be nearly identical or have negligible differences.

3.4.3. Hardness Test

In Fig. 18, the hardness data analysis showed a significant drop in Vickers hardness values following the implementation of the RS method (the reason for applying RS was to increase density by reducing porosity), resulting in a decrease to below the 350–400 HV range. Prior to RS, the material demonstrated substantially higher hardness, typically within the 550–650 HV range (samples with the condition of E_0^* <17). Generally, an increase in E_0^* corresponds to a slight decrease in hardness. This situation can be understood through two distinct scenarios.

These variations in hardness data can serve as evidence of a coarser microstructure that appears when the hardness decreases according to the Hall-Petch relation (Armstrong, 1970), as well as martensitic transformation caused by CR, as discussed in the XRD section. As acicular shape martensite α' phase exhibits harder characteristics, especially on Ti64, compared to its β phase (Vrancken et al., 2012). Alloying elements that stabilize the α phase were assumed primarily found in α sub-grains, resulting in an element-deficient α' phase in lamellar sections, thereby causing significant differences in hardness (fluctuations) and strength between the $\alpha + \beta$ lamellae (Lütjering, 1998). Additionally, metal oxidation can alter hardness, as O_2 impacts α phase stabilizers (Shen et al., 2019). Metals naturally tend to oxidize, and this O_2 uptake during fabrication might explain unexpected increases in hardness values, especially since all processes were conducted with an argon re-circulation system. Moreover, these large fluctuations may occur due to small porosities beneath (or near) the indent location as it will absorb the pressure; therefore, a small indent area which could lead to high hardness.

4. Conclusion

This research explored the use of multiple low-power 450 nm diode lasers to melt Ti-6Al-4V powder and create high-density diode area melted samples. The fabrication of single-track, single-layer, and multi-layer structures demonstrated that melt pool dynamics were altered by laser orientation (perpendicular to the scanning direction), resulting in wide melt pools around 1100 μm. This introduced a new phenomenon in the multi-laser approach PBF explained as the "crescent effect." The employment of short wavelength lasers enhanced laser absorption, enabling the creation of samples with 99.3% density using low power (4 W each), coupled with the implementation of a rescanning strategy to counteract the crescent effect. A parameter map plotting normalized energy density (E_0^*) was developed, showing that an energy density of E_0^* > 20.5 creates the highest-density samples. The importance of cooling rate (CR) in the DAM system is explained as CR decreases whenever energy density increases. Microstructural examination revealed the presence of lamellar $\alpha + \beta$ phases throughout the sample along the build direction. Furthermore, acicular martensite α' structures were observed closer to the top surface of samples due to the higher CRs. Hardness testing showed that the rescanning strategy led to a decline in hardness values (from around 550 HV to around 350 HV), indicative of a coarser microstructure. However, when compared to traditional LPBF systems, the material still exhibited relatively high hardness values. β peaks appeared above the E_0^* = 8 region. Interestingly, with the lowest CR sample, the diffraction peaks broadened, indicating that residual stress might have occurred.

CRediT authorship contribution statement

Halil Caglar: Conceptualization, Methodology, Validation, Formal analysis, Investigation, Writing - original draft, Visualization. Anqi Liang: Methodology, Writing – review & editing. Kristian Groom: Conceptualization, Supervision. Kamran Mumtaz: Conceptualization, Project administration, Supervision, Writing – review & editing.

Declaration of Competing Interest

I wish to affirm that this research paper submission is original and is not concurrently under consideration for publication elsewhere.

Acknowledgment

References

C. Additive, "PowderRange Ti64 Datasheet." Accessed: Jan. 20, 2024. [Online]. Available: ⟨https://www.carpentertechnology.com/alloy-finder/powderrange-ti64⟩.

Ahmed, T., Rack, H.J., 1998. Phase transformations during cooling in α+β titanium alloys. Mater. Sci. Eng.: A 243 (1–2), 206–211. https://doi.org/10.1016/s0921-5093(97)00802-2.

Ali, H., Ghadbeigi, H., Mumtaz, K., 2018. Effect of scanning strategies on residual stress and mechanical properties of Selective Laser Melted Ti6Al4V. Mater. Sci. Eng. A 712, 175–187. https://doi.org/10.1016/j.msea.2017.11.103.

Alsaddah, M., Khan, A., Groom, K., Mumtaz, K., 2021. Use of 450-808 nm diode lasers for efficient energy absorption during powder bed fusion of Ti6Al4V. Int. J. Adv. Manuf. Technol. 113, 2461–2480. https://doi.org/10.1007/s00170-021-06774-4.

Alsaddah, M., Khan, A., Groom, K., Mumtaz, K., 2022. Diode area melting of Ti6Al4V using 808 nm laser sources and variable multi-beam profiles. Mater. Des. 215, 110518 https://doi.org/10.1016/j.matdes.2022.110518.

Armstrong, R.W., 1970. The influence of polycrystal grain size on several mechanical properties of materials. Met. Mater. Trans. B (5), 1169–1176. https://doi.org/10.1007/bf02900227.

Capozzi, L.C., Sivo, A., Bassini, E., 2022. Powder spreading and spreadability in the additive manufacturing of metallic materials: a critical review. J. Mater. Process. Technol. 308, 117706 https://doi.org/10.1016/j.jmatprotec.2022.117706.

Gaillard, Q., Boulnat, X., Cazottes, S., Dancette, S., Desrayaud, C., 2023. Strength/ductility trade-off of laser powder bed fusion Ti-6Al-4V: synergetic effect of alpha-case formation and microstructure evolution upon heat treatments. Addit. Manuf. 76, 103772 https://doi.org/10.1016/j.addma.2023.103772.

Gates-Rector, B. T, 2019. "04-020-7055, the powder diffraction file: a quality materials characterization database. no. 34 Powder Diffr. (4), 352–360. https://doi.org/10.1017/s0885715619000812.

Gates-Rector, Blanton, S., 2019. "00-044-1294, the powder diffraction file: a quality materials characterization database. no. 34 Powder Diffr. (4), 352–360. https://doi.org/10.1017/s0885715619000812.

Gong, J., Wei, K., Liu, M., Song, W., Li, X., Zeng, X., 2022. Microstructure and mechanical properties of AlSi10Mg alloy built by laser powder bed fusion/direct energy deposition hybrid laser additive manufacturing. Addit. Manuf. 59, 103160 https://doi.org/10.1016/j.addma.2022.103160.

Khairallah, S.A., Anderson, A.T., Rubenchik, A., King, W.E., 2016. Laser powder-bed fusion additive manufacturing: physics of complex melt flow and formation mechanisms of pores, spatter, and denudation zones. Acta Mater. 108, 36–45. https://doi.org/10.1016/j.actamat.2016.02.014.

Liang, A., Pey, K.S., Polcar, T., Hamilton, A.R., 2022. Effects of rescanning parameters on densification and microstructural refinement of 316L stainless steel fabricated by laser powder bed fusion. J. Mater. Process. Technol. 302, 117493 https://doi.org/10.1016/j.jmatprotec.2022.117493.

Liu, Y., Yang, Y., Wang, D., 2016. A study on the residual stress during selective laser melting (SLM) of metallic powder. Int. J. Adv. Manuf. Technol. 87, 647–656. https://doi.org/10.1007/s00170-016-8466-y.

Lütjering, G., 1998. Influence of processing on microstructure and mechanical properties of (α+β) titanium alloys. Mater. Sci. Eng.: A 243 (1–2), 32–45. https://doi.org/10.1016/s0921-5093(97)00778-8.

Matthews, M.J., et al., 2017. Diode-based additive manufacturing of metals using an optically-addressable light valve. Opt. Express 25, 11788. https://doi.org/10.1364/oe.25.011788.

Miao, X., Wu, M., Han, J., Li, H., Ye, X., 2020. Effect of laser rescanning on the characteristics and residual stress of selective laser melted titanium Ti6Al4V alloy. Materials 13 (18), 3940. https://doi.org/10.3390/ma13183940.

Owen, L., 2022. Powder Refinement - opening the black box. Univ. Sheff. 1–20.

Pathania, A., Subramaniyan, A.K., Nagesha, B.K., 2022. Influence of post-heat treatments on microstructural and mechanical properties of LPBF-processed Ti6Al4V alloy. Prog. Addit. Manuf. 7 (6), 1323–1343. https://doi.org/10.1007/s40964-022-00306-6.

Shen, X.-J., Zhang, C., Yang, Y.-G., Liu, L., 2019. On the microstructure, mechanical properties and wear resistance of an additively manufactured Ti64/metallic glass composite. Addit. Manuf. 25, 499–510. https://doi.org/10.1016/j.addma.2018.12.006.

Shipley, H., et al., 2018. Optimisation of process parameters to address fundamental challenges during selective laser melting of Ti-6Al-4V: a review. Int. J. Mach. Tools Manuf. 128, 1–20. https://doi.org/10.1016/j.ijmachtools.2018.01.003.

Simonelli, M., Tse, Y.Y., Tuck, C., 2014. The formation of α + β microstructure in as-fabricated selective laser melting of Ti–6Al–4V. J. Mater. Res. 29 (17), 2028–2035. https://doi.org/10.1557/jmr.2014.166.

Singla, A.K., et al., 2021. Selective laser melting of Ti6Al4V alloy: process parameters, defects and post-treatments. J. Manuf. Process. 64, 161–187. https://doi.org/10.1016/j.jmapro.2021.01.009.

Song, B., Dong, S., Zhang, B., Liao, H., Coddet, C., 2012. Effects of processing parameters on microstructure and mechanical property of selective laser melted Ti6Al4V. Mater. Des. 35, 120–125. https://doi.org/10.1016/j.matdes.2011.09.051.

Thijs, L., Verhaeghe, F., Craeghs, T., Humbeeck, J.V., Kruth, J.-P., 2010. A study of the microstructural evolution during selective laser melting of Ti–6Al–4V. Acta Mater. 58, 3303–3312. https://doi.org/10.1016/j.actamat.2010.02.004.

Thomas, M., Baxter, G.J., Todd, I., 2016. Normalised model-based processing diagrams for additive layer manufacture of engineering alloys. Acta Mater. 108, 26–35. https://doi.org/10.1016/j.actamat.2016.02.025.

Vrancken, B., Thijs, L., Kruth, J.-P., Humbeeck, J.V., 2012. Heat treatment of Ti6Al4V produced by selective laser melting: microstructure and mechanical properties. J. Alloy. Compd. 541, 177–185. https://doi.org/10.1016/j.jallcom.2012.07.022.

Wu, S.Q., et al., 2016. Microstructural evolution and microhardness of a selective-laser-melted Ti–6Al–4V alloy after post heat treatments. J. Alloy. Compd. 672, 643–652. https://doi.org/10.1016/j.jallcom.2016.02.183.

Xiao, Z., Chen, C., Hu, Z., Zhu, H., Zeng, X., 2020. Effect of rescanning cycles on the characteristics of selective laser melting of Ti6Al4V. Opt. Laser Technol. 122, 105890 https://doi.org/10.1016/j.optlastec.2019.105890.

Young, Z.A., et al., 2020. Types of spatter and their features and formation mechanisms in laser powder bed fusion additive manufacturing process. Addit. Manuf. 36, 101438 https://doi.org/10.1016/j.addma.2020.101438.

Zavala-Arredondo, M., et al., 2017. Laser diode area melting for high speed additive manufacturing of metallic components. Mater. Des. 117, 305–315. https://doi.org/10.1016/j.matdes.2016.12.095.

Zhang, T., et al., 2018. Evolution of molten pool during selective laser melting of Ti–6Al–4V. J. Phys. D: Appl. Phys. 52 (5), 055302 https://doi.org/10.1088/1361-6463/aaee04.